Catalysis Today 437 (2024) 114749

Contents lists available at ScienceDirect

Catalysis Today

journal homepage: www.elsevier.com/locate/cattod

# Fluoride-etched $TiO_2$ microspheres modified with $Al_2O_3$ for enhanced photocatalytic conversion of $NO_x$ into nitrate ions

Tarek A. Kandiel [a,b,*], Muhammad Kamran [a], Mohamed A. Morsy [a,c], Detlef W. Bahnemann [d], Amira Y. Ahmed [e]

[a] Department of Chemistry, King Fahd University of Petroleum & Minerals (KFUPM), Dhahran 31261, Saudi Arabia
[b] Interdisciplinary Research Center for Hydrogen Technologies and Carbon Management (IRC-HTCM) at KFUPM, Dhahran 31261, Saudi Arabia
[c] Interdisciplinary Research Center for Construction & Building Materials (IRC-CBM), King Fahd University of Petroleum & Minerals (KFUPM), Dhahran 31261, Saudi Arabia
[d] Laboratory "Photoactive Nanocomposite Materials", Saint-Petersburg State University, Ulyanovskaya str. 1, Peterhof, Saint-Petersburg 198504, Russia
[e] Department of Chemistry, Faculty of Science, Sohag University, Sohag 82524, Egypt

ARTICLE INFO

*Keywords:*
$NO_x$ abatement, $TiO_2$ microspheres
Nitrate selectivity
EPR analysis
Hole trapping sites, Photocatalysis

ABSTRACT

Photocatalysis holds promise for the removal of $NO_x$ from the air, yet its limited selectivity toward desired products (e.g. nitrate ions) hinders its widespread application. In this study, we synthesized and comprehensively characterized amorphous $TiO_2$ microspheres (ATMS), fluoride-etched TMS (F-TMS), and $Al_2O_3$-modified F-TMS ($Al_2O_3$/F-TMS) photocatalysts. The photocatalytic $NO_x$ abatement tests revealed negligible photoactivity for the TMS, with significant improvement observed after the fluoride ions etching using the hydrothermal method. However, the selectivity of F-TMS for $NO_x$ removal remained lower than that of $TiO_2$ P25. The $Al_2O_3$/F-TMS photocatalyst exhibited a substantial increase in selectivity. The analysis of $NO_x$ abatement results indicated a 2.7-fold boost in selectivity compared to $TiO_2$ P25. A reasonable correlation between the amount of chemically absorbed water and nitrate selectivity was observed. The electron paramagnetic resonance (EPR) disclosed that the fluoride etching induced the formation of intra-band-gap hole-trapping sites and thus enhanced the photocatalytic activity. Nevertheless, the selectivity improvement was mainly attributed to $Al_2O_3$'s ability to stabilize the $NO_x$ oxidation intermediates at the surface for subsequent oxidation to nitrate ions. This study provides valuable insights for tailoring photocatalysts to enhance both activity and selectivity in photocatalytic $NO_x$ abatement.

## 1. Introduction

Presently, the environment is facing serious problems concerning air pollution. It's mainly due to the burning of fossil fuels, and exhaust toxic gases from industries and vehicles, causing major environmental issues in the world. This creates too many problems for human, animal, and planet lives. Air pollution has been classified into primary and secondary classes according to their origin. The primary air pollution is due to the emission of carbon monoxide (CO), nitrogen oxides, sulfur dioxide ($SO_2$), and solid particles. Chemical reactions in the atmosphere cause the second class of air pollution such as ozone ($O_3$), sulfuric acid ($H_2SO_4$), and nitric acid ($HNO_3$) [1–3]. Nitrogen monoxide (NO) and nitrogen dioxide ($NO_2$) commonly referred to as $NO_x$ are among the major causes of air pollution. The annual mean concentration of $NO_x$ globally is around 20–90 ppb but the hourly average sometimes goes to 1000 ppb in high-traffic urban areas [4]. The recommended value of $NO_x$ emission by the agencies of environmental protection should be $\leq$0.2 ppm [5]. The increasing concentration of $NO_x$ is affecting global lives and needs sustainable and inexpensive technology to resolve this environmental issue.

In this regard, photocatalysis has attracted much attention due to its promising results in $NO_x$ abatement in construction materials, e.g. photocatalytic paints and concrete [6,7]. $TiO_2$ [8–11], ZnO [12], $WO_3$ [13], $Bi_2WO_6$ [14], and g-$C_3N_4$ [15–17] photocatalysts have commonly been tested for the removal of $NO_x$. Recently, a new class of photocatalysts such as $BaSO_4$ with engineered Ba-vacancy [18], eosin Y reassembled Ti-based metal-organic framework (MOF, $NH_2$-MIL-125 (Ti)) [19], and Eu-doped $Zn_2Al$-$CO_3$ layered double hydroxide [20] have

* Corresponding author at: Department of Chemistry, King Fahd University of Petroleum & Minerals (KFUPM), Dhahran 31261, Saudi Arabia
*E-mail addresses:* tarek.kandiel@kfupm.edu.sa, kandiel@science.sohag.edu.eg (T.A. Kandiel).

https://doi.org/10.1016/j.cattod.2024.114749
Received 27 November 2023; Received in revised form 13 February 2024; Accepted 21 April 2024
Available online 29 April 2024

been also employed for the photocatalytic $NO_x$ removal. Among these photocatalysts, $TiO_2$ is still attractive due to its excellent physical and chemical properties, low cost, and non-toxicity. Moreover, it has a proper band structure for oxygen reduction and $^{\bullet}OH$ radicals generation by oxidizing adsorbed water or surface hydroxyl groups [21]. Although about 90 % of the photogenerated electron/hole pairs recombine within 10 ns [9], the photocatalysis process is still promising for systems in which the degradation of pollutants in ppm levels such as in the case of $NO_x$ removal. However, the main challenge for utilizing the photocatalytic process for the removal of $NO_x$ is the poor selectivity toward desired products, i.e. nitrate ions [22]. The surface modification of $TiO_2$ either by grafting with metal ions (e.g. $Fe^{3+}$) [23] or loading with metal oxides (e.g. $Al_2O_3$) [24,25] was shown an improved selectivity toward $NO_x$ removal. This was mainly attributed to the improved rate of photocatalytic $NO_2$ oxidation. The fluorination of $TiO_2$ was reported to improve the photocatalytic activity due to the enhanced rate of $^{\bullet}OH$ radicals generation in the aqueous phase [26]. It was also reported that it facilitates the desorption of $^{\bullet}OH$ radicals at the air/catalyst interface thus enhancing the photoactivity [27]. Inspired by these reports, we synthesized amorphous $TiO_2$ microspheres (ATMS), and then we etched them with fluoride ions to improve their photocatalytic activity toward NO oxidation. To enhance the selectivity, the fluoride-etched $TiO_2$ microspheres (F-TMS) were modified with an amorphous $Al_2O_3$ layer ($Al_2O_3$/F-TMS). The photocatalytic $NO_x$ abatement results indicated that the $Al_2O_3$/F-TMS sample exhibits higher activity and 2.7-fold boosted nitrate selectivity than the benchmark photocatalyst (i.e. Evonik $TiO_2$ P25). The electron paramagnetic resonance (EPR) indicates that the improved photocatalytic activity might be attributed to the formation of hole-trapping sites after the etching step. Whereas the improved selectivity is more likely due to the $Al_2O_3$'s ability to stabilize the $NO_x$ oxidation intermediate at the surface for subsequent oxidation to nitrate ions.

## 2. Experimental section

### 2.1. Synthesis of amorphous $TiO_2$ microspheres (ATMS)

The amorphous $TiO_2$ microspheres were synthesized according to the literature after modification [28]. An equal volume of butyl alcohol and acetonitrile (Sigma Aldrich, total volume 250 ml) was mixed very well in an Erlenmeyer flask at 35 C for five minutes. Then 3.12 ml of ammonium hydroxide solution (Sigma Aldrich, 28 %) was added, and then 5.0 ml of titanium (IV) isopropoxide (TTIP, Sigma Aldrich) was promptly injected into the above solution under vigorous stirring. After continuous stirring at 1000 rpm for three hours at 25 C, the $TiO_2$ microspheres product was centrifuged and washed two times with ethanol and dried in an oven overnight at 70 ℃. The yield for ATMS formation was approximately 100 %.

### 2.2. Synthesis of fluoride-etched $TiO_2$ Microspheres (F-TMS)

For the synthesis of F-TMS, 0.5 g of the ATMS was dispersed in 50 ml of double distilled water, and then 0.032 g of sodium fluoride (Sigma Aldrich) was added to the suspension. After continuous stirring at 700 rpm for one hour at room temperature, 0.15 g of polyvinylpyrrolidone (PVP, average molecular weight 10k, Sigma Aldrich) was added and the mixture was further stirred for another hour. After that, the suspension was transferred into a 100 ml Teflon-lined autoclave and heated at 110 ℃ for 4 hours in a drying oven. The final product was washed two times with double distilled water and then dried at 110 ℃. It was further calcined at 300 ℃ for 2 hours (ramping rate 5 °C/min) to remove carbon residual from the used precursor before the photocatalytic test. The obtained F-TMS mass was 0.35 g (yield 70%).

### 2.3. Modification of F-TMS with $Al_2O_3$ layer

The as-prepared F-TMS were modified with $Al_2O_3$ by the impregnation method. In a typical experiment, the desired amount of aluminum ethoxide (Sigma Aldrich) required to have 2.0, 5.0, or 10 wt % of $Al_2O_3$ was dissolved in 25 ml of 0.1 M acetic acid ethanolic solution. Then, 0.15 g of the F-TMS was added to the mixture and stirred at 700 rpm for one hour. After that, the mixture was heated to 70 ℃ to evaporate all the ethanol. The resulting product was then collected and calcined at 300 ℃ for 2 hours to ensure the formation of $Al_2O_3$. The temperature ramping rate was 5 °C/min. The resulting product is named hereafter $Al_2O_3$/F-TMS photocatalyst and the yield was close to 100 %.

### 2.4. Photocatalytic $NO_x$ abatement ISO test

The $NO_x$ abatement was conducted according to the ISO standard 22197–1 test [29]. 100 mg of the photocatalyst was dispersed in 0.5 ml of double distilled water and drop-cased on a glass plate (total coated area 24 $cm^2$). After that, the photocatalyst film was dried at 50 C for 3 hours and exposed to UV(A) light (365 nm) for 12 hours before the $NO_x$ test to clean the surface and remove the adsorbed adventitious organic compounds. The description for the photocatalytic $NO_x$ abatement setup is fully given in ref. [11]. The concentration of NO concentration was 1000±50 ppb and the flow rate was 3.0 L $min^{-1}$ with 50 % humidity. The concentration of NO and $NO_2$ were analyzed by using a Teledyne NOx analyzer (Model T200). The 365 nm Thorlab LED is used as a light source and the light intensity was adjusted to 1.0 mW/$cm^2$ using a calibrated photodiode (FDS100-CAL, Thorlabs). For the test under simulated solar light, the ABET solar simulator (Model 11002 SunLite) was used and the light intensity was adjusted to 1.0 sun using a calibrated silicon reference cell (ABET Technologies). The photonic efficiencies (ξ) of NO oxidation, $NO_2$ generation, and $NO_x$ removal in a time interval from $t_0$ and $t_1$ and UV(A) light illumination were calculated from Eq. 1, and the selectivity (S) of $NO_x$ removal from Eq. 2 [10].

$$\xi = \frac{n_{molecules}}{n_{photons}} = \frac{\int_{t_0}^{t_1} AXdt}{I\,(t_1 - t_0)} \quad (1)$$

$$S\,(\%) = \frac{\xi_{NO_x}}{\xi_{NO}} \times 100 \quad (2)$$

The gas flow coefficient constant (A) was $2.045\times10^{-12}$ mol $s^{-1}$, X is the amount of oxidized NO, generated $NO_2$, or removed $NO_x$ in ppb, and I is the incident photon flux (Einstein $s^{-1}$).

For the nitrate ions analysis, the photocatalyst, after the test completion, was dispersed in deionized water and stirred for 30 min. Then, the suspension was filtered using a Millipore PTE 0.2 μm syringe filter, diluted to the desired volume, and analyzed by ion chromatography.

### 2.5. EPR and TGA measurements

X-Band electron paramagnetic resonance (EPR) spectra were measured at low temperature (-150 °C) in situ on a MiniScope MS300 EPR spectrometer (Magnettech GmbH, Germany), upgraded with a frequency meter (ADANI CMS8400's) and fast registry functioned. The full details of the system are described in ref. [11] and in the supporting information. The thermal gravimetric (TGA) measurements were conducted using a TA-SDT Q600 thermogravimetric thermal analyzer. A ~7.0 mg of all the materials was heated in an alumina crucible in an $N_2$ atmosphere at a 20 ml/min flow rate. The temperature ramping rate was 10 °C/min until reached 120 °C, then isothermal at 120 °C for 10 min, and then increased to 500 °C with a ramping rate of 20 °C/min.

### 2.6. Characterization

The details of the analysis techniques (i.e. X-ray diffraction, scanning electron microscopy, transmission electron microscopy, Raman, diffuse reflectance spectroscopy, and ion chromatography) are given in the supporting information.

## 3. Results and discussion

### 3.1. Characterization of the photocatalysts

The X-ray diffraction (XRD) patterns of all photocatalysts are displayed in Fig. 1a. The diffraction peaks of ATMS confirmed its amorphous nature. The hydrothermal etching and calcination of ATMS at 300 °C leads to the formation of mainly anatase $TiO_2$ (PDF card No. 00–021–1272). A trace amount of brookite was observed after the hydrothermal etching as evinced from the small diffraction peak located at 2θ=30.8°. The modification of F-TMS with different loadings of $Al_2O_3$ (i.e. 2.0, 5.0, 10 wt %) decreased the intensity of the anatase diffraction peak indicating the successful modification at the surface with the $Al_2O_3$ layer. No peaks were detected for $Al_2O_3$ indicating its amorphous nature. The crystallite sizes of F-TMS and 5.0 wt % $Al_2O_3$/F-TMS were determined from the Williamson-Hall analysis of the XRD patterns [30]. The Williamson-Hall plot is presented in Figures S1a and b, respectively. It was found that both samples exhibit almost the same crystallite size of 17 nm. This is expected since both samples have been treated under the same hydrothermal and thermal conditions. The Raman spectra of the F-TMS and 5.0 wt % $Al_2O_3$/F-TMS samples further confirmed the formation of anatase $TiO_2$ (Fig. 1b). Both samples have the main peaks of anatase $TiO_2$ located at around 146, 397, 516, and 638 $cm^{-1}$ which can be assigned to the $E_g$, $B_{1g}$, (doublet of $A_{1g}$+ $B_{1g}$), and $E_g$ vibrational modes [31]. The modification of the F-$TiO_2$ sample with $Al_2O_3$ enhanced significantly the Raman intensity indicating the electronic interaction between $Al_2O_3$ and $TiO_2$.

The SEM and TEM images of ATMS, F-TMS, and 5.0 wt % $Al_2O_3$/F-TMS photocatalysts are given in Fig. 2. For $Al_2O_3$/F-TMS photocatalyst modified with 2.0 and 10.0 wt % $Al_2O_3$, the SEM and TEM images are given in Fig S2 and S3. The SEM results reveal that the ATMS has a spherical shape and an average diameter of ~185 nm (Fig. 2a). The fluoride etching turns the solid $TiO_2$ microspheres into an urchin-like porous structure (Fig. 2b). The modification with $Al_2O_3$ has a little impact on the apparent morphology of the F-TMS as seen from Fig. 2c. The TEM images presented in Fig. 2d, e, and f further confirmed the spherical and urchin-like structures of ATMS, F-TMS, and $Al_2O_3$ modified F-TMS photocatalysts. The $N_2$ adsorption/desorption isotherms of the synthesized $TiO_2$ materials are shown in Fig. 3a. It shows that the ATMS exhibits type-Ib isotherm and micropore structure due to the formation of highly-packed solid sphere particles. The F-TMS exhibited type-IV isotherm indicating the formation of a mesoporous structure due to the etching and nanostructuring of the solid spheres [32]. The modification of The F-TMS sample with $Al_2O_3$ has further improved the mesoporosity. The pore-size distribution was calculated using the Barrett-Joyner-Halenda (BJH) method and presented in Fig. S4. It showed that all samples modified with $Al_2O_3$ showed a narrow range of pore-size distribution with an average of 7.0 nm, but the etched $TiO_2$ sample had a broader range of pore-size distribution due to the nanostructuring by etching. It seems that the loading of $Al_2O_3$ to the etched $TiO_2$ surfaces blocks the large pores and induces the formation of mesoporous materials. The calculated BET surface areas are shown in Fig. 3b.

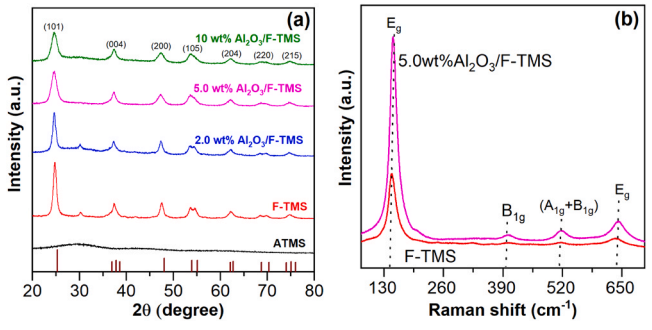


**Fig. 1.** (a) XRD patterns of ATMS, F-TMS, and $Al_2O_3$-modified F-TMS photocatalysts ($Al_2O_3$ loadings: 2.0, 5.0, 10 wt %), the verticle lines denote the Bragg peak positions (PDF card No. 00–021–1272), the lattice planes denote the peak with highest intensity when peaks are overlapped; (b) Raman spectra of F-TMS and 5.0 wt%$Al_2O_3$/F-TMS photocatalysts.

The XPS analysis of the $Al_2O_3$/F-TMS showed the characteristic peaks of $TiO_2$ at 458 and 463.7 eV that can be assigned for Ti $2p_{3/2}$ and Ti $2p_{1/2}$, respectively (Fig. S5a). These two peaks are accountable for the lattice tetravalent titanium ion ($Ti^{4+}$) [33,34]. The deconvolution of Ti 2p resulted in a shoulder peak at 458.8 eV indicating the plausible existence of $Ti^{3+}$ species [35]. Fig. S5b presents the XPS spectra of oxygen (O 1 s). It showed a broad peak centered at 527 eV and can be assigned to M-O-M and the adsorbed oxygen species [36]. The peak observed at 681.0 eV in the binding energy region of F 1 s confirmed the presence of fluoride species [37]. The Al 2p XPS spectrum presented in Fig. 4b can be readily deconvoluted into two peaks located at 71.9 and 75.2 eV that can be assigned to $Al_2O_3$ and Al metal, respectively. The formation of Al metal has been previously observed for the calcined $Al_2O_3$ single crystal [38]. The bandgap of the prepared photocatalysts was determined by measuring their diffuse reflectance spectra (DRS, Fig. 5). All samples except the ATMS have the same absorption onset. Assuming indirect bandgap transition [39], the Tau plot for the 5.0 wt % $Al_2O_3$/F-TMS photocatalyst was plotted as an example which resulted in a band gap of 3.2 eV. This value is the typical value reported for anatase $TiO_2$ [39].

### 3.2. Photocatalytic $NO_x$ abatement

The concentration-time profiles of the photocatalytic $NO_x$ abatement over $TiO_2$-P25, ATMS, F-TMS, and $Al_2O_3$-modified F-TMS photocatalysts are depicted in Fig. 6(a-f). Each profile is divided into three stages. Stage 1 represents the NO equilibrium over the photocatalysis in the dark. Stage 2 represents the UV(A) illumination period (2 hours). In this stage NO is either oxidized to $NO_2$ or removed. The sum of NO and $NO_2$ concentration is displayed as $NO_x$. In stage 3, after two hours of illumination, the light is switched off and the reaction is kept to reach the dark equilibrium again. The photonic efficiencies were calculated according to Eq. 1 and presented in Fig. 7a. It is worth reminding here that all samples have been calcined at 300 °C except the ATMS sample. For adequate comparison, the ATMS has also been calcined at 300 °C and tested but it showed negligible activity. The hydrothermal fluoride etching step was crucial for improving activity.

As shown in Fig. 6, the ATMS exhibited negligible photocatalytic activity. But, after etching with fluoride ions and calcination at 300 °C, the photocatalytic activity is significantly enhanced. It is known that the fluorination of the $TiO_2$ surface modifies its surface properties by replacing the surface hydroxyl groups with fluoride ions and improves its photocatalytic activity via the formation of intra-band-gap energy states close to the valance band [40]. Despite the photocatalytic activity of the F-TMS photocatalyst having been improved relative to that of ATMS, its selectivity towards $NO_x$ is still lower than that of $TiO_2$ P25. The photocatalytic oxidation of NO to nitrate ($NO_3^-$) or nitric acid ($HONO_2$) over $TiO_2$ photocatalysts is a complex multi-step process as illustrated in Eqs. 3–12 [11,41]. Assuming that the conduction band electron ($e_{cb}^-$) and the valance band hole ($h_{vb}^+$) will be able to diffuse to the surface and get involved in the photocatalytic process, a highly reactive oxygen species (ROS) will be formed (Eqs. 4–6)

$$TiO_2 + UV(A) \rightarrow TiO_2(h_{VB}^+ + e_{CB}^-) \quad (3)$$

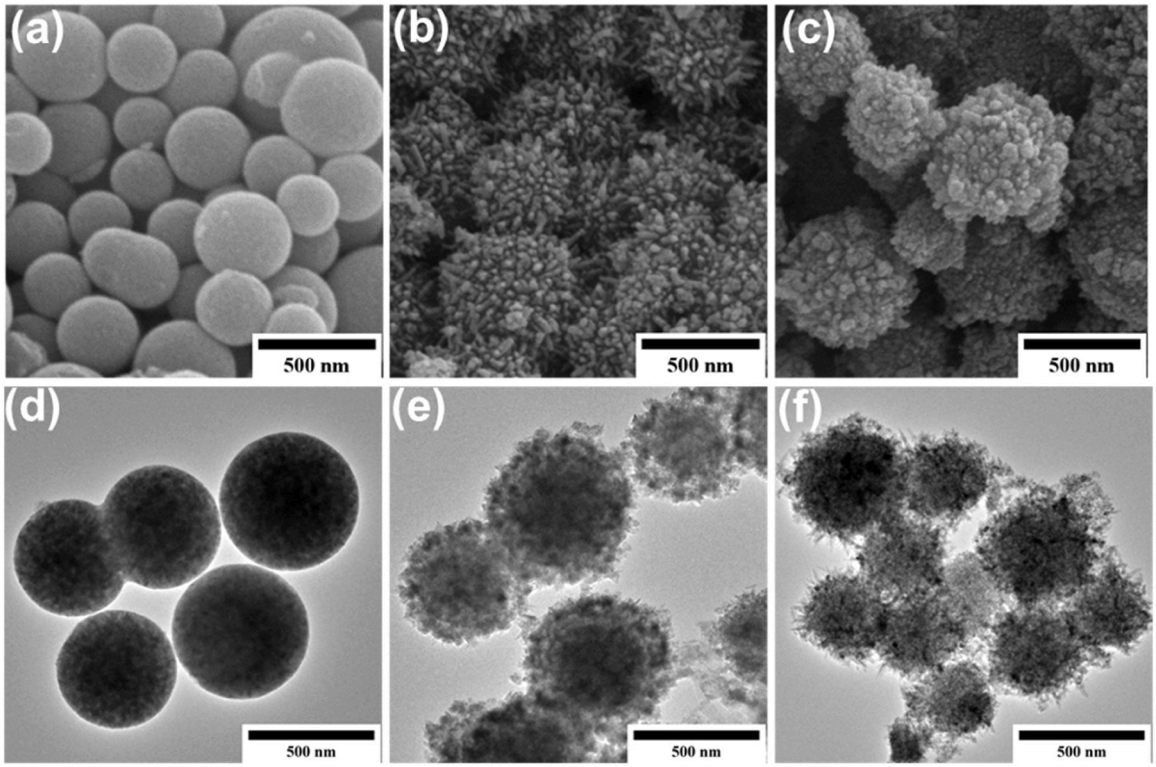


**Fig. 2.** SEM and TEM images of ATMS (a, d), F-TMS (b, e), and 5.0 wt % $Al_2O_3$/F-TMS photocatalysts (c, f), respectively.

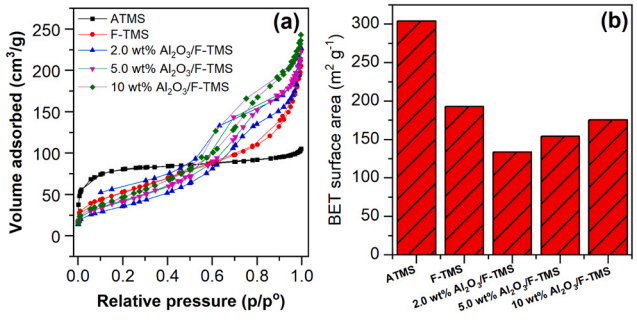


**Fig. 3.** (a) $N_2$ adsorption/desorption isotherms and (b) BET surface area of ATMS, F-TMS, and $Al_2O_3$-modified F-TMS photocatalysts ($Al_2O_3$ loadings: 2.0, 5.0, 10 wt %).

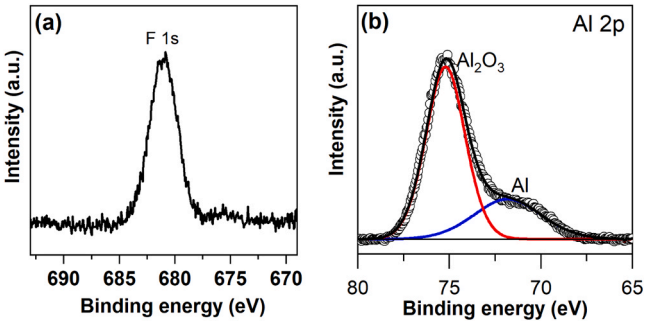


**Fig. 4.** High-resolution XPS spectra of F 1 s (a) and Al 2p (b) core levels in 5.0 wt % $Al_2O_3$ modified F-TMS photocatalyst.

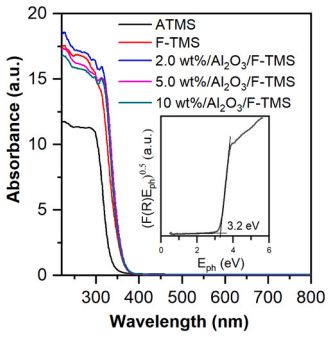


**Fig. 5.** DRS of ATMS, F-TMS, and $Al_2O_3$-modified F-TMS photocatalysts ($Al_2O_3$ loadings: 2.0, 5.0, and 10 wt %). The inset shows Tauc's plot of the 5.0 wt % $Al_2O_3$ modified F-TMS photocatalyst.

$$TiO_2(e^-_{CB}) + O_{2,ads} \rightarrow O^{\bullet -}_{2,ads} + TiO_2 \quad (4)$$

$$TiO_2(h^+_{VB}) + H_2O_{ads} \rightarrow TiO_2 + {}^{\bullet}OH_{ads} + H^+ \quad (5)$$

$$TiO_2(h^+) + TiO_2(O_{br}) \rightarrow TiO_2(O^{\bullet}_{br}) \quad (6)$$

These ROS can oxidize NO to $NO_2$ either by $^{\bullet}OH$ radicals and trapped holes (Eqs. 7 and 8) or by $O^{\bullet -}_2$ (Eq. 9).

$$NO_{ads} \xrightarrow{{}^{\bullet}OH_{ads}\,HNO_2} \xrightarrow{{}^{\bullet}OH_{ads}\,NO_{2,ads}+H_2O} \quad (7)$$

$$NO_{ads} \xrightarrow{TiO_2(O^{\bullet}_{br}),\ H_2O_{ads}} TiO_2 + NO_{2,ads} + 2H^+ \quad (8)$$

$$NO_{ads} \xrightarrow{O^{\bullet -}_{2ads},H^+} NO_{2,ads} + {}^{\bullet}OH_{ads} \quad (9)$$

In a less acidic environment, the reaction of $O^{\bullet -}_{2\ ads}$ with $NO_{ads}$ might lead to peroxynitrite intermediate ($ONOO^-$) formation which undergoes

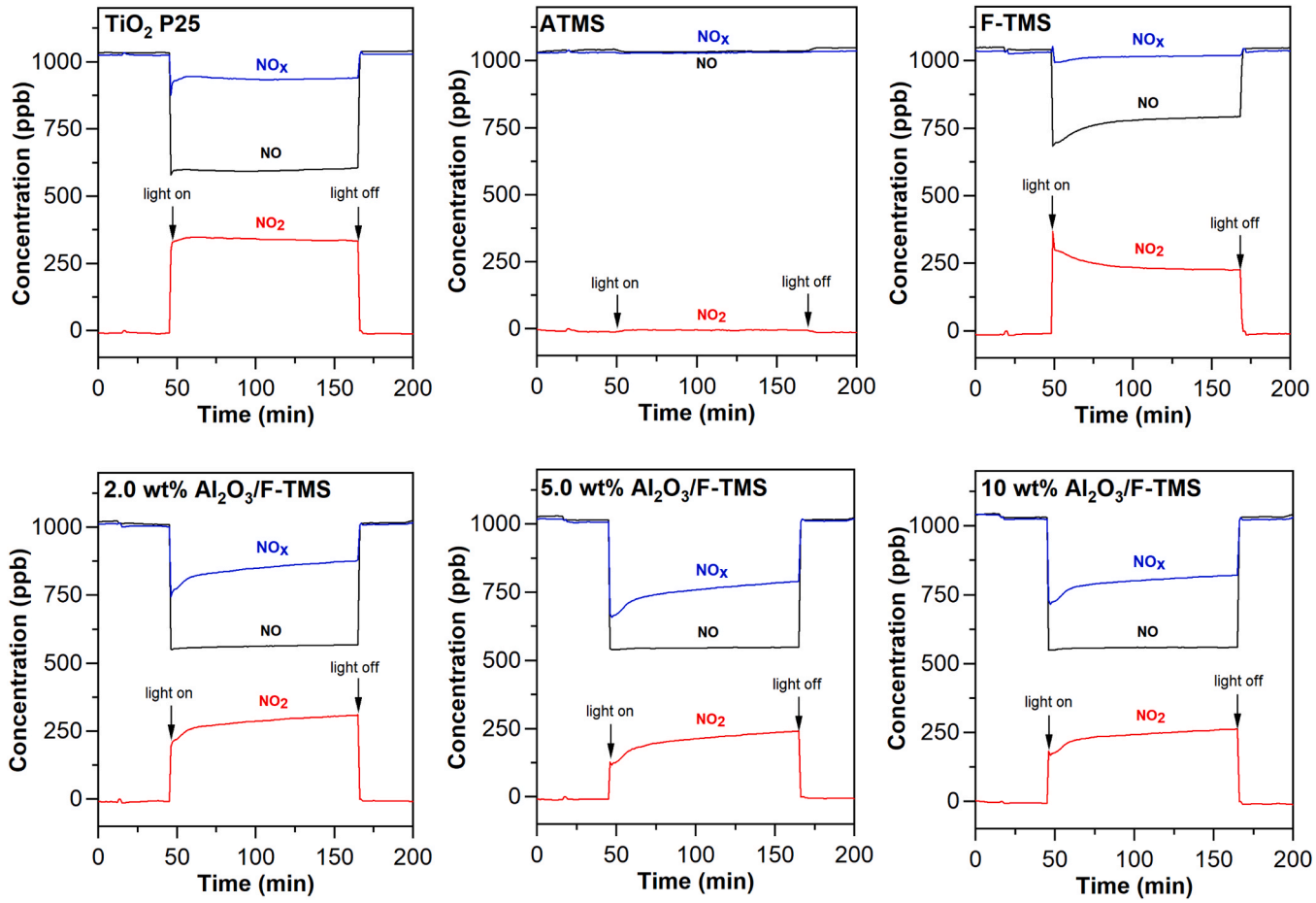


**Fig. 6.** Concentration-time profiles of photocatalytic $NO_x$ abatement over $TiO_2$ P25, ATMS, F-TMS, and $Al_2O_3$-modified F-TMS photocatalysts ($Al_2O_3$ loadings: 2.0, 5.0, 10 wt %).

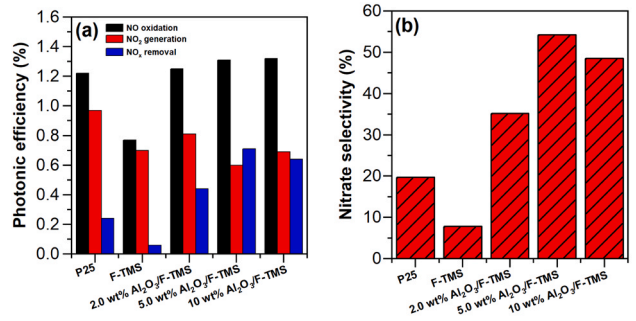


**Fig. 7.** Photonic efficiency (a) and selectivity to nitrate ions formation (b) of photocatalytic $NO_x$ abatement over $TiO_2$ P25, F-TMS, and $Al_2O_3$-modified F-TMS photocatalysts ($Al_2O_3$ loadings: 2.0, 5.0, 10 wt %).

rearrangement to produce $NO_3^-$ ions (Eq. 10). The nitrate ions formation can also be achieved by the oxidation of generated $NO_2$ using either $^{\bullet}OH$ radicals (Eq. 11) or trapped holes (Eq. 12).

$$NO_{ads} \xrightarrow{O^{\bullet-}_{2,ads}} ONOO^- \rightarrow NO_3^- \quad (10)$$

$$NO_{2,ads} + {}^{\bullet}OH_{ads} \rightarrow HNO_{3,ads} \quad (11)$$

$$NO_{2,ads} \xrightarrow{TiO_2(O^{\bullet}_{br}),\ H_2O_{ads}} TiO_2 + NO^-_{3,ads} + 2H^+ \quad (12)$$

According to these equations, the adsorbed water, the surface acidity, and the type of generated holes (free $^{\bullet}OH$ radical or trapped holes) play a vital role in the photocatalytic oxidation of $NO_x$. It is worth mentioning here that the synthesized ATMS photocatalyst is etched with fluoride ions and thus it is highly expected that the F-TMS photocatalyst has a fluorinated surface and also surface defects (hole trapping sites) as proven by the EPR analysis (Section 3.3). The fluorination of $TiO_2$ surface facilitates the desorption of $^{\bullet}OH$ radicals at the air/catalyst interface thus enhancing the photoactivity as previously reported [27]. The creation of hole-trapping sites also increases the photocatalytic activity [42,43]. This agrees with the improved photocatalytic activity observed after the fluoride etching of the TMS. But the selectivity was still lower than that of $TiO_2$ P25. To improve the selectivity toward the formation of nitrate ions, the generated $NO_x$ oxidation intermediates should be stored at the surface for further oxidation. As previously reported, $Al_2O_3$ can store $NO_x$ at the surface and thus allows the steps illustrated in Eqs. 7–11 to occur to a greater extent [24,25]. $Al_2O_3$ has also a higher point of zero charge than that of $TiO_2$ [44] and thus it is less acidic than $TiO_2$. This environment might promote the formation of nitrate ions according to Eq. 10 and inhibit the reaction given in Eq. 9. Indeed, upon the modification of the F-TMS photocatalyst with $Al_2O_3$, the selectivity toward nitrate ion formation has been significantly improved (Fig. 7b). Interestingly, the 5.0 wt % $Al_2O_3$ modified F-TMS photocatalyst showed 2.7-fold higher selectivity than $TiO_2$ P25 for nitrate ions formation. It can be observed from Fig. 7 that, despite the selectivity having been improved, the NO conversion is almost the same for the $TiO_2$ P25 and the $Al_2O_3$-modified F-TMS photocatalysts. This might be attributed to the mass transport effect as previously proposed for the ISO 22197–1 reactor [45]. To investigate this possibility, the photocatalytic activity has been measured at a higher flow rate (4.5 L $min^{-1}$) to minimize the mass transport effect (Fig. S6). The photonic efficiency of NO conversion

at this flow rate has been calculated and found to be 1.26 %. This value is almost equal to that calculated at a flow rate of 3.0 L $min^{-1}$ evincing that the mass transport has a limited effect under our experimental condition. To assure the nitrate formation, the amount of nitrate ions formed after the $NO_x$ abatement test was determined using ionic chromatography. In acceptable agreement with the amount of $NO_x$ removed (3.8 μmol), the concentration of nitrate ions formed on the 5.0 wt % $Al_2O_3$ modified F-TMS photocatalyst was found to be 3.0 μmol. The IR spectrum was also recorded after the test and presented in Fig. S7. It shows clearly the characteristic peak of nitrate ions located at 1384 $cm^{-1}$. To test the stability and the performance of the developed catalyst, a 5-hour run was performed under simulated solar light (AM1.5 G, 1.0 sun, F.g. 8 1st run). However, the NO conversion was stable over the 5-hour test, the $NO_2$ concentration gradually increased over time (which means less selectivity for nitrate ions). This is attributed to the mediation of NO oxidation through Eq. 13 instead of Eq. 10 as previously reported [45]. This is understood due to the accumulation of nitrate ions in the form of nitric acid. We collected the photocatalyst after this test and washed it with water then retested it again as a fresh sample. The results are shown in Fig. 8 2nd run and indicated that the NO conversion activity is decreased by approximately 12 %. Moreover, the $NO_x$ removal is rapidly dropped which is more likely due to dissolving the $Al_2O_3$ layer by the generated nitric acid during the washing.

$$2NO + O_2 \xrightarrow{HNO_3} 2NO_2 \quad (13)$$

### 3.3. TGA and EPR analysis

The adsorbed water and defects (electron and hole trapping sites) play a significant role in the photocatalytic $NO_x$ abatement process [41–43]. The thermogravimetric analysis (TGA) helps to investigate the effect of physiosorbed and chemosorbed water molecules on the surface of synthesized $TiO_2$ photocatalysts. The TGA results are shown in Fig. 9. It has been divided into two steps. Step 1 represents the weight loss due to the desorption of physically adsorbed water (temperature up to 120 °C), and step 2 represents the weight loss due to the desorption of chemically bounded water (temperature up to 500 °C) [46]. The analysis of step 1 indicated that the amounts of physical adsorbed water are 0.9, 11.0, 3.8, 4.2, and 5.0 mmole $g^{-1}$ for $TiO_2$ P25, ATMS, F-TMS, and $Al_2O_3$-modified F-TMS ($Al_2O_3$ loadings: 2.0, 5.0, 10 wt %) photocatalysts, respectively. Normalizing these values to the BET surface area indicated that the amounts of water adsorbed per unit area are 16.4, 36.2, 19.8, 17.9, 27.2, and 28.3 μmole $m^{-2}$. The analysis of step 2 indicated that the amounts of chemically adsorbed water were 9.7, 9.6, 6.9, 14.4, 14.3, and 12.7 μmole $m^{-2}$ for $TiO_2$ P25, TMS, F-TMS, and $Al_2O_3$ loaded F-TMS ($Al_2O_3$ loadings: 2.0, 5.0, 10 wt %) photocatalysts, respectively. A correlated trend between the amount of chemically adsorbed water and selectivity is observed (Fig. S8). This indeed assures that water is required as a proton source for nitric acid formation and also the generation of •OH radicals. But, one should mention here that the photocatalysis process is complex and depends on many other parameters. For instance, the ATMS photocatalyst exhibits an amount of chemically adsorbed water comparable to that of $TiO_2$ P25 but it showed negligible photocatalytic activity.

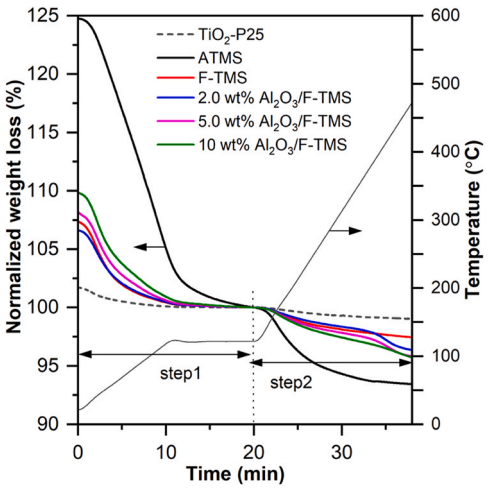


**Fig. 9.** Normalized TGA curves of $TiO_2$ P25, TMS, F-TMS, and $Al_2O_3$-modified F-TMS photocatalysts ($Al_2O_3$ loadings: 2.0, 5.0, 10 wt %).

As discussed above, the formation of defects (electron and hole trapping sites) could affect the activity and selectivity of $NO_x$ abatement over $TiO_2$ photocatalysts. Here we have investigated this possibility by conducting low-temperature (-150 °C) EPR analysis and the results are depicted in Fig. 10. The TMS has two main peaks, one at g = 1.9420 due to the electrons tapped at the $Ti^{4+}$ sites as $Ti^{3+}$ (trapped electrons) [47]. The other peak, located at g = 2.0007, can be assigned to the surface trapped holes as $[Ti^{4+}O^{-\bullet}Ti^{4+}OH^-]$ [48]. After the etching of the ATMS, new peaks appeared at g = 2.0212, g = 2.0470, and g = 2.0614. These peaks can be assigned to the intra-band-gap hole trapping sites with the structure of $[Ti^{4+}O^{2-}Ti^{4+}O^{-\bullet}]$ [48]. This agrees with the reported finding that the fluorination of $TiO_2$ induces the formation of intra-band-gap energy states close to the valance band [40]. As reported, they are localized at intra-band-gap energy levels within approximately 1.3 eV above the valence band. The EPR peaks assigned to the intra-band-gap energy states were not observed in the $TiO_2$ P25 sample. $TiO_2$ P25 consists of a mixture of rutile and anatase phases, and the synergy between these two phases is commonly believed to be the reason for its high photocatalytic activity [49]. Based on the EPR and photocatalytic results it can be concluded that the trapped holes play a key role in the improvement of the photocatalytic $NO_x$ abatement but still, $Al_2O_3$ modification is required for improving selectivity toward nitrate ions formation.

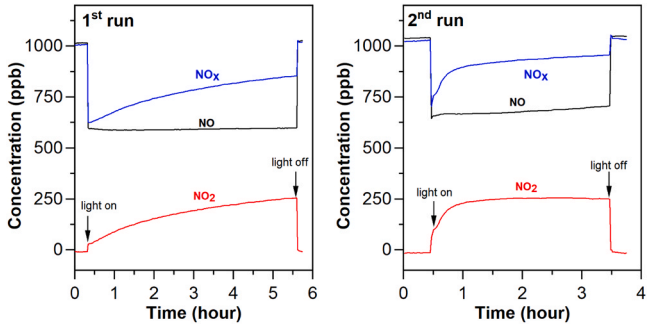


**Fig. 8.** Concentration-time profiles of photocatalytic $NO_x$ abatement over 5.0 wt %$Al_2O_3$/F-TMS photocatalyst under standard solar irradiation (AM1.5 G, 1.0 sun).

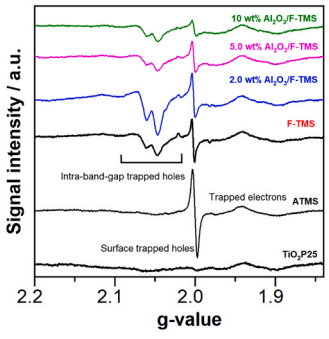


**Fig. 10.** EPR spectra of $TiO_2$ P25, TMS, F-TMS, and $Al_2O_3$-modified F-TMS photocatalysts ($Al_2O_3$ loadings: 2.0, 5.0, 10 wt %).

## 4. Conclusion

Amorphous $TiO_2$ microspheres (ATMS) were synthesized through the controlled hydrolysis of titanium(IV) isopropoxide in the presence of ammonium hydroxide. Despite the ATMS initially exhibiting negligible activity for the photocatalytic abatement of $NO_x$, hydrothermal etching with fluoride ions led to significantly enhanced photocatalytic activity. However, the selectivity toward $NO_x$ removal remained lower than that of the benchmark $TiO_2$ P25. The fluoride-etched TMS photocatalyst (F-TMS) was subsequently modified with $Al_2O_3$, resulting in a significant improvement in the selectivity toward $NO_x$ removal. The analysis of the $NO_x$ abatement results revealed that the $Al_2O_3$-loaded F-TMS exhibited a 2.7-fold increase in selectivity compared to $TiO_2$ P25. A correlated trend between the amount of chemically absorbed water and the selectivity was observed based on the thermal gravimetric analysis. The electron paramagnetic resonance measurements proved that fluoride-etching induces the formation of intra-band-gap hole-trapping sites, thereby improving photocatalytic activity. However, the primary factor contributing to selectivity improvement was attributed to the ability of $Al_2O_3$ to stabilize the $NO_x$ oxidation intermediates at the surface for further oxidation to nitrate ions.

## CRediT authorship contribution statement

**Tarek A. Kandiel:** Methodology, Investigation, Conceptualization, Supervision, Writing – original draft. **Muhammad Kamran:** Methodology, Investigation, Writing – original draft. **Mohamed A. Morsy:** Methodology, Supervision, Writing – review & editing. **Detlef W. Bahnemann:** Writing – review & editing. **Amira Y. Ahmed:** Writing – review & editing, Conceptualization.

## Declaration of Competing Interest

The authors declare that they have no known competing financial interests or personal relationships that could have appeared to influence the work reported in this paper.

## Data Availability

Data will be made available on request.

## Acknowledgments

The authors acknowledge the support provided by the Deanship of Scientific Research (DSR) at King Fahd University of Petroleum & Minerals (KFUPM) through Project No. DF181025.

## Appendix A. Supporting information

Supplementary data associated with this article can be found in the online version at doi:10.1016/j.cattod.2024.114749.

## References

[1] I. Manisalidis, E. Stavropoulou, A. Stavropoulos, E. Bezirtzoglou, Environmental and health impacts of air pollution: a review, Front. Public Health (2020) 14.
[2] J. Ângelo, L. Andrade, L.M. Madeira, A. Mendes, An overview of photocatalysis phenomena applied to $NO_x$ abatement, J. Environ. Manag. 129 (2013) 522–539.
[3] H. Orru, K. Ebi, B. Forsberg, The interplay of climate change and air pollution on health, Curr. Environ. Health Rep. 4 (2017) 504–513.
[4] J.A. Mendoza, D.H. Lee, J.-H. Kang, Photocatalytic removal of $NO_x$ using $TiO_2$-coated zeolite, Environ, Eng. Res. 21 (2016) 291–296.
[5] A. Folli, S.B. Campbell, J.A. Anderson, D.E. Macphee, Role of $TiO_2$ surface hydration on NO oxidation photo-activity, J. Photochem. Photobiol. A Chem. 220 (2011) 85–93.
[6] M. Baudys, R. Andrews, R. Han, C. O'Rourke, S. Hodgen, J. Krysa, A. Mills, Photocatalytic paints for $NO_x$ removal: influence of various weathering conditions, J. Environ. Chem. Eng. 9 (2021) 106172.
[7] L. Yang, A. Hakki, F. Wang, D.E. Macphee, Photocatalyst efficiencies in concrete technology: the Effect of photocatalyst placement, Appl. Catal. B Environ. 222 (2018) 200–208.
[8] E. Luévano-Hipólito, A.M. de la Cruz, Enhancement of photocatalytic properties of $TiO_2$ for NO photo-oxidation by optimized sol–gel synthesis, Res. Chem. Intermed. 42 (2016) 7065–7084.
[9] M. Xu, Y. Bao, K. Wu, T. Xia, H.L. Clack, H. Shi, V.C. Li, Influence of $TiO_2$ incorporation methods on $NO_x$ abatement in Engineered Cementitious Composites, Constr. Build. Mater. 221 (2019) 375–383.
[10] L. Yang, A. Hakki, L. Zheng, M.R. Jones, F. Wang, D.E. Macphee, Photocatalytic concrete for $NO_x$ abatement: supported TiO2 efficiencies and impacts, Cem. Concr. Res. 116 (2019) 57–64.
[11] M. Kamran, T.A. Kandiel, S. Abdel-Azeim, M.A. Morsy, D.W. Bahnemann, Mechanistic insights into the high selectivity and photocatalytic activity of brookite $TiO_2$ Toward $NO_x$, Abat. J. Phys. Chem. C 127 (2023) 7707–7717.
[12] X. Chen, H. Zhang, D. Zhang, Y. Miao, G. Li, Controllable synthesis of mesoporous multi-shelled ZnO microspheres as efficient photocatalysts for NO oxidation, Appl. Surf. Sci. 435 (2018) 468–475.
[13] P. Dong, N. Xu, Y. Xu, X. Wang, A study of $Pt/WO_3$-carrier catalysts for photocatalytic purification of NO gas, Catal. Commun. 84 (2016) 142–146.
[14] L. Zhang, C. Yang, K. Lv, Y. Lu, Q. Li, X. Wu, Y. Li, X. Li, J. Fan, M. Li, SPR effect of bismuth enhanced visible photoreactivity of Bi2WO6 for NO abatement, Chin. J. Catal. 40 (2019) 755–764.
[15] F. Dong, Y. Li, Z. Wang, W.-K. Ho, Enhanced visible light photocatalytic activity and oxidation ability of porous graphene-like g-$C_3N_4$ nanosheets via thermal exfoliation, Appl. Surf Sci. 358 (2015) 393–403.
[16] Y. Sun, W. Zhang, T. Xiong, Z. Zhao, F. Dong, R. Wang, W.-K. Ho, Growth of BiOBr nanosheets on $C_3N_4$ nanosheets to construct two-dimensional nanojunctions with enhanced photoreactivity for NO removal, J. Colloid Interface Sci. 418 (2014) 317–323.
[17] M. Irfan, M. Sevim, Y. Koçak, M. Balci, Ö. Metin, E. Ozensoy, Enhanced photocatalytic $NO_x$ oxidation and storage under visible-light irradiation by anchoring $Fe_3O_4$ nanoparticles on mesoporous graphitic carbon nitride (mpg-$C_3N_4$), Appl. Catal. B Environ. 249 (2019) 126–137.
[18] W. Cui, L. Chen, J. Li, Y. Zhou, Y. Sun, G. Jiang, S.C. Lee, F. Dong, Ba-vacancy induces semiconductor-like photocatalysis on insulator $BaSO_4$, Appl. Catal. B Environ. 253 (2019) 293–299.
[19] M. Xu, Y. Xu, C. Zhang, S. Chen, X. Liu, H. Wu, S. Li, Y. He, F. Dong, A novel defect reassembly strategy for $NH_2$-MIL-125(Ti) to enhance the photocatalytic NO removal activity, Sep. Purif. Technol. 322 (2023) 124374.
[20] A. Pastor, C. Chen, G. de Miguel, F. Martín, M. Cruz-Yusta, D. O'Hare, I. Pavlovic, L. Sánchez, Facile synthesis of visible-responsive photocatalytic Eu-doped layered double hydroxide for selective removal of $NO_x$ pollutant, Chem. Eng. J. 471 (2023) 144464.
[21] A. Kubacka, M. Fernandez-Garcia, G. Colon, Advanced nanoarchitectures for solar photocatalytic applications, Chem. Rev. 112 (2012) 1555–1614.
[22] J.Z. Bloh, A. Folli, D.E. Macphee, Photocatalytic $NO_x$ abatement: why the selectivity matters, RSC Adv. 4 (2014) 45726–45734.
[23] J. Patzsch, Jacob N. Spencer, A. Folli, J.Z. Bloh, Grafted iron(iii) ions significantly enhance $NO_2$ oxidation rate and selectivity of $TiO_2$ for photocatalytic NOx abatement, RSC Adv. 8 (2018) 27674–27685.
[24] M. Çağlayan, M. Irfan, K.E. Ercan, Y. Kocak, E. Ozensoy, Enhancement of photocatalytic $NO_x$ abatement on titania via additional metal oxide $NO_x$-storage domains: interplay between surface acidity, specific surface area, and humidity, Appl. Catal. B Environ. 263 (2020) 118227.
[25] A.M. Soylu, M. Polat, D.A. Erdogan, Z. Say, C. Yıldırım, Ö. Birer, E. Ozensoy, $TiO_2$–$Al_2O_3$ binary mixed oxide surfaces for photocatalytic NOx abatement, Appl. Surf. Sci. 318 (2014) 142–149.
[26] C. Minero, G. Mariella, V. Maurino, D. Vione, E. Pelizzetti, Photocatalytic transformation of organic compounds in the presence of inorganic ions. 2. Competitive reactions of phenol and alcohols on a titanium dioxide−fluoride system, Langmuir 16 (2000) 8964–8972.
[27] H. Kim, W. Choi, Effects of surface fluorination of TiO2 on photocatalytic oxidation of gaseous acetaldehyde, Appl. Catal. B Environ. 69 (2007) 127–132.
[28] J.H. Pan, X.Z. Wang, Q. Huang, C. Shen, Z.Y. Koh, Q. Wang, A. Engel, D. W. Bahnemann, Large-scale synthesis of Urchin-like mesoporous $TiO_2$ hollow spheres by targeted etching and their photoelectrochemical properties, Adv. Funct. Mater. 24 (2013) 95–104.
[29] A. Mills, S. Elouali, The nitric oxide ISO photocatalytic reactor system: measurement of $NO_x$ removal activity and capacity, J. Photochem. Photobiol. A Chem. 305 (2015) 29–36.
[30] D.H. Manh, T.T. Ngoc Nha, L.T. Hong Phong, P.H. Nam, T.D. Thanh, P.T. Phong, Determination of the crystalline size of hexagonal $La_{1-x}Sr_xMnO_3$ (x = 0.3) nanoparticles from X-ray diffraction – a comparative study, RSC Adv. 13 (2023) 25007–25017.
[31] U. Balachandran, N.G. Eror, Raman spectra of titanium dioxide, J. Solid State Chem. 42 (1982) 276–282.
[32] J.H. Pan, X.Z. Wang, Q. Huang, C. Shen, Z.Y. Koh, Q. Wang, A. Engel, D. W. Bahnemann, Large-scale synthesis of urchin-like mesoporous $TiO_2$ hollow spheres by targeted etching and their photoelectrochemical properties, Adv. Funct. Mater. 24 (2014) 95–104.
[33] G.C. Vásquez, M.A. Peche-Herrero, D. Maestre, B. Alemán, J. Ramirez-Castellanos, A. Cremades, J.M. Gonzalez-Calbet, J. Piqueras, Influence of Fe and Al doping on the stabilization of the anatase phase in TiO 2 nanoparticles, J. Mater. Chem. C 2 (2014) 10377–10385.

[34] L. Yang, N. Feng, F. Deng, Aluminum-doped $TiO_2$ with dominant {001} Facets: microstructure and property evolution and photocatalytic, Act. J. Phys. Chem. C 126 (2022) 5555–5563.
[35] Y. Xu, S. Wu, P. Wan, J. Sun, Z.D. Hood, Introducing $Ti^{3+}$ defects based on lattice distortion for enhanced visible light photoreactivity in TiO2 microspheres, RSC Adv. 7 (2017) 32461–32467.
[36] J.-C. Dupin, D. Gonbeau, P. Vinatier, A. Levasseur, Systematic XPS studies of metal oxides, hydroxides and peroxides, Phys. Chem. Chem. Phys. 2 (2000) 1319–1324.
[37] J.I. Brauer, G. Szulczewski, Important role of surface fluoride in nitrogen-doped $TiO_2$ nanoparticles with visible light photocatalytic activity, J. Phys. Chem. B 118 (2014) 14188–14195.
[38] T. Tago, N. Kataoka, H. Tanaka, K. Kinoshita, S. Kishida, XPS study from a clean surface of $Al_2O_3$ single crystals, Procedia Eng. 216 (2017) 175–181.
[39] T.A. Kandiel, A. Feldhoff, L. Robben, R. Dillert, D.W. Bahnemann, Tailored titanium dioxide nanomaterials: anatase nanoparticles and brookite nanorods as highly active photocatalysts, Chem. Mater. 22 (2010) 2050–2060.
[40] N. Fessi, M.F. Nsib, L. Cardenas, C. Guillard, F. Dappozze, A. Houas, F. Parrino, L. Palmisano, G. Ledoux, D. Amans, Y. Chevalier, Surface and electronic features of fluorinated $TiO_2$ and their influence on the photocatalytic degradation of 1-methylnaphthalene, J. Phys. Chem. C 124 (2020) 11456–11468.
[41] L. Yang, A. Hakki, F. Wang, D.E. Macphee, Different roles of water in photocatalytic $DeNO_x$ mechanisms on $TiO_2$: basis for engineering nitrate selectivity? ACS Appl. Mater. Interfaces 9 (2017) 17034–17041.
[42] H. Shang, M. Li, H. Li, S. Huang, C. Mao, Z. Ai, L. Zhang, Oxygen vacancies promoted the selective photocatalytic removal of NO with blue $TiO_2$ via simultaneous molecular oxygen activation and photogenerated hole annihilation, Environ. Sci. Technol. 53 (2019) 6444–6453.
[43] J. Ma, H. Wu, Y. Liu, H. He, Photocatalytic removal of $NO_x$ over visible light responsive oxygen-deficient $TiO_2$, J. Phys. Chem. C 118 (2014) 7434–7441.
[44] M. Kosmulski, The pH dependent surface charging and points of zero charge. VIII Update, Adv. Colloid Interface Sci. 275 (2020) 102064.
[45] A. Mills, L. Burns, C. O'Rourke, S. Elouali, Kinetics of the photocatalysed oxidation of NO in the ISO 22197 reactor, J. Photochem. Photobiol. A Chem. 321 (2016) 137–142.
[46] R. Mueller, H.K. Kammler, K. Wegner, S.E. Pratsinis, OH surface density of $SiO_2$ and $TiO_2$ by thermogravimetric analysis, Langmuir 19 (2003) 160–165.
[47] C.P. Kumar, N.O. Gopal, T.C. Wang, M.-S. Wong, S.C. Ke, E.P.R. Investigation, of $TiO_2$ nanoparticles with temperature-dependent properties, J. Phys. Chem. B 110 (2006) 5223–5229.
[48] N.O. Gopal, H.-H. Lo, T.-F. Ke, C.-H. Lee, C.-C. Chou, J.-D. Wu, S.-C. Sheu, S.-C. Ke, Visible light active phosphorus-doped $TiO_2$ nanoparticles: an EPR evidence for the enhanced charge, Sep. J. Phys. Chem. C 116 (2012) 16191–16197.
[49] R. Su, R. Bechstein, L. Sø, R.T. Vang, M. Sillassen, B. Esbjörnsson, A. Palmqvist, F. Besenbacher, How the Anatase-to-Rutile ratio influences the photoreactivity of $TiO_2$, J. Phys. Chem. C 115 (2011) 24287–24292.